Originally published as:

Scaling of maximum observed magnitudes with geometrical and stress properties of strike-slip faults

Patricia Martínez-Garzón[1], Marco Bohnhoff[1,2], Yehuda Ben-Zion[3], and Georg Dresen[1,4]

[1]GFZ German Research Centre for Geosciences, Potsdam, Germany, [2]Institute of Geological Sciences, Free University of Berlin, Berlin, Germany, [3]Department of Earth Sciences, University of Southern California, Los Angeles, California, USA, [4]Institute of Earth and Environmental Sciences, University of Potsdam, Potsdam, Germany

Abstract We test potential scaling between observed maximum earthquake magnitudes along 27 strike-slip faults with various properties including cumulative displacement, mapped fault length, seismogenic thickness, slip rates, and angle between fault strike and maximum horizontal stress. For 75–80% of the data set, the observed maximum scalar moment scales with the product of seismogenic thickness and either cumulative displacement or mapped fault length. Most faults from this population have slip rates >5 mm/yr (interplate faults), cumulative displacement >10 km, and relatively high angles to the maximum horizontal stress orientation. The remaining 20–25% population involves events at some distance from a plate boundary with slip rate <5 mm/yr, cumulative displacements <10 km, and ≈45° to the maximum horizontal stress. These earthquakes have larger magnitudes than the previous population, likely because of larger stress drops. The most likely interpretation of the results is that the maximum rupture length, and hence earthquake magnitudes, correlates with the cumulative displacement and the fault surface length. The results also suggest that progressive fault smoothing may lead to decreasing coseismic stress drops.

1. Introduction

Large continental strike-slip faults such as the San Andreas Fault in California or the North Anatolian Fault in Turkey are known to produce earthquakes with magnitudes up to ~*M*8. Such events pose a substantial seismic hazard since they are typically shallow (<20 km) and may occur in densely populated regions such as the Los Angeles Basin, San Francisco Bay area, or Istanbul metropolitan region. Thus, providing constraints on the maximum likely earthquake magnitude along these faults is of major relevance and can improve the seismic hazard estimation and associated risk. Currently, there is no method to systematically estimate the maximum earthquake magnitude on a given fault.

Instrumental earthquake catalogs generally cover only up to approximately 150 years, which is substantially less than the typical recurrence time between major earthquakes [e.g., *Parsons*, 2004; *Ben-Zion*, 2008]. As a consequence, the largest observed magnitude that occurred along a particular fault (hereafter referred as M_{MAX}^{obs}) was not always recorded instrumentally. Historical records of damage for areas with long settlement history have been used to characterize large shakings and likely M_{MAX} [e.g., *Ben-Menahem*, 1991; *Ambraseys and Jackson*, 1998; *Petersen et al.*, 2015; *Albini et al.*, 2013]. Alternatively, M_{MAX} can be estimated from paleoseismic trenching or measuring the slope failures in lakes [e.g., *Strasser et al.*, 2006]. The uncertainties in the inferred M_{MAX}^{obs} values vary substantially depending on the method used for its estimation and the region.

The moment magnitude M_W [*Hanks and Kanamori*, 1979] based on the scalar seismic moment is defined as follows:

$$M_W = \frac{2}{3}\log(\mu \cdot \Delta u \cdot A) - 6, \tag{1}$$

where μ is the rigidity in the source volume, Δu is the average coseismic slip, and A is the rupture area. For large earthquakes (e.g., $M \geq 6.5$) it can be assumed that the entire seismogenic crust fails [*Pacheco and Sykes*, 1992] and thus A becomes the product of the earthquake rupture length R_L and seismogenic thickness z. The value of z can be considered approximately constant for a given region, although it may vary along large

faults. A similar expression could be formulated based on the scalar seismic potency given by the seismic moment divided by rigidity [*Ben-Zion and Zhu*, 2002]. We therefore do not address the rigidity in the subsequent discussion and assume it to be constant for the considered faults.

As the fault zone evolves with increasing deformation, the structural heterogeneities (e.g., number of steps per unit length) tend to decrease [*Tchalenko*, 1970; *Wesnousky*, 1988; *Stirling et al.*, 1996; *Wechsler et al.*, 2010; *Brodsky et al.*, 2011] and larger through-going individual ruptures are possible [*Ben-Zion and Sammis*, 2003; *Wechsler et al.*, 2010]. Consequently, the available length R_L for rupturing in an earthquake is expected to increase with fault evolution, suggesting that M_{MAX}^{obs} may also increase [*Wesnousky*, 1988]. A compilation of source parameters from historical earthquakes [*Wells and Coppersmith*, 1994] shows that Δu roughly scales with R_L, consistent with crack-like models with constant stress drop [e.g., *Scholz*, 1982; *Ben-Zion*, 2008; *Shaw*, 2009]. This observation has been used in developing scaling relations between rupture geometry, displacement, and seismic moment [e.g., *Leonard*, 2010].

Analysis of fault parameters may provide information on the available rupture area and contribute to constraining M_{MAX}^{obs}. Such parameters include the total mapped surface fault length (L_f), depth of the seismogenic layer (z) estimated from high-precision hypocenter catalogs or GPS measurements, and cumulative fault displacement (C_d) measured from geological or morphological markers combining information on the fault age and average slip rate. The parameter L_f is expected to increase as the fault grows and develops [e.g., *Kim and Sanderson*, 2005] although estimates might suffer from nonuniform mapping resolutions. A scaling relation is observed between C_d and L_f for unbounded faults in similar rock types and faulting regime [*Cowie and Scholz*, 1992a, 1992b].

In this study we provide a compilation of data on M_{MAX}^{obs} along continental strike-slip faults in combination with information on various geometrical properties to investigate their potential scaling and discuss the possibility of providing constraints on M_{MAX}^{obs}. We find that M_{MAX}^{obs} scales logarithmically with the product of seismogenic depth and cumulative displacement for 75% of the total data set and with the product of seismogenic depth and mapped fault length for 80% of the data set. Most faults fitting this population are at a plate boundary and have $C_d > 10$ km, slip rate >5 mm/yr, and an angle >50° with respect to the regional maximum horizontal stress (S_{HMAX}). The remaining 20–25% of the analyzed faults hosted larger earthquakes than suggested by the relation for most faults. These faults are typically distant from a plate boundary, have $C_d > 10 km$, slip rate <5 mm/yr, an angle of about 45° from S_{HMAX} and tend to rupture with comparatively larger stress drops.

2. Catalog Compilation

We compile a catalog from 27 continental strike-slip faults worldwide focusing on the maximum observed earthquake magnitude (M_{MAX}^{obs}), fault geometry, and the average angle between the fault strike and regional S_{HMAX} (ψ). Note that the maximum observed earthquake magnitude along a certain fault provides only a lower bound on the maximum possible earthquake on that fault. While the results are associated necessarily with limited information, they still provide useful comparative information for probabilistic estimations. The considered geometrical parameters are C_d, z, and L_f defined in section 1. Information on the slip rates is also compiled. When M_{MAX}^{obs} occurred within the instrumental period, we also compile its earthquake rupture length (R_L) and average coseismic slip (Δu) [e.g., *Wells and Coppersmith*, 1994]. Some faults are subdivided into individual sections if different sets $C_d / M_{MAX}^{obs} / \psi / z$ are available. This results in 29 major fault sections worldwide (Figure 1a). Each fault is identified in different figures with a particular fault ID number as specified in Table S1.

The range of earthquake magnitudes included in this catalog varies from ~ $M_W 6.5$ to ~ $M_W 8$. The M_{MAX} at each fault (section) is converted to moment magnitude M_W if possible using the relation between M_s and M_W from *Scordilis* [2006], $M_W \approx M_s + 0.1$, site-dependent relations between local magnitude M_L and M_W (e.g., for faults in China or New Zealand, see individual fault descriptions in Text S1), or the relation between M_{JMA} and M_W as described in *Utsu* [1999] for faults in Japan. The reported M_{MAX} uncertainties vary depending on how the magnitudes were estimated, e.g., recorded instrumentally, from paleoseismic studies or from historical intensity reports. The latter is related to the event date, the fault remoteness from civilization settlements, the research on that fault performed during the instrumental period, and the provided
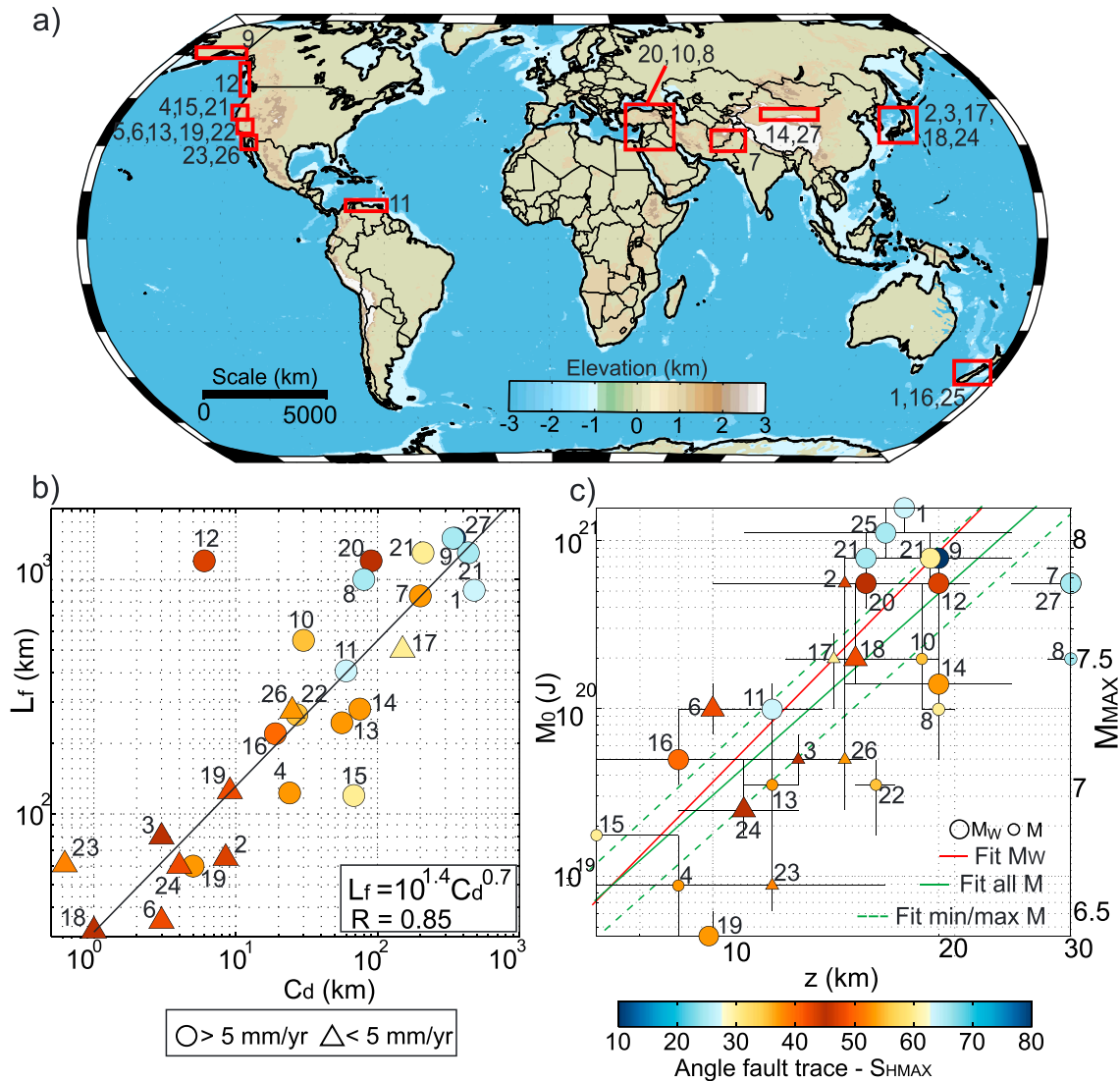
Figure 1. (a) Location of the 27 analyzed continental strike-slip fault zones. (b) Relation between cumulative displacement (C_d) and mapped fault length (L_f). (c) Relation between seismogenic thickness (z), moment magnitude (M_0), and maximum magnitude (M_{MAX}^{obs}). Size of the data points is encoded with the magnitude type. Red line: logarithmic fit using observations with M_W. Green solid line: logarithmic fit of all points. Green dashed lines: logarithmic fit to the maximum and minimum magnitudes, respectively. For Figures 1b and 1c numbers represent fault IDs as listed in Table S1. Color is encoded with angle ψ between fault trace and maximum horizontal stress S_{HMAX}. Circle symbols represent faults with slip rates >5 mm/yr, while triangles represent faults with slip rate <5 mm/yr.

magnitude type of each event. Each case is evaluated separately attending to these factors. Parameters derived for each fault (section) and their uncertainties are provided in Table S1. Details on all the faults used in this study and the relevant references are given in Text S1.

The seismogenic thickness z is typically defined as the depth down to which 90–95% of the local seismicity occurs using the best available seismicity catalogs for the region (e.g., *Waldhauser and Schaff* [2008] and *Hauksson et al.* [2012] for Northern and Southern California, respectively). We also compare the seismogenic thickness from seismicity with the estimated locking depth from GPS measurements whenever data are available (see Text S1). To only consider the seismic portion of the crust, correction for fault creep is also performed when information is available (e.g., for the Hayward Fault).

3. Results

All faults considered here are associated with a dominant strike-slip faulting regime. The data set comprises faults in different rock types that are either bounded (displacement goes to the zero at the fault tip) or

possibly unbounded. A scaling relation between the mapped fault length L_f and cumulative displacement C_d is expected generally only for bounded faults where progressive displacement results in increasing fault length [*Cowie and Scholz*, 1992a, 1992b]. Nevertheless, the compiled data with potentially unbounded faults indicate a scaling relation in the form $L_f = 10^{1.4} C_d^{0.7}$ (Figure 1b). The exception is the Fairweather Fault (ID = 12 in Figure 1b), which has remarkably low C_d for its L_f value. Most short faults with small C_d and slip rates <5 mm/yr are oriented at about $\psi = 40$–$50°$ to S_{HMAX} close to the orientation of maximum resolved shear stress. In contrast, faults with large C_d and L_f typically have smaller (Dead Sea Transform and Median Tectonic Line, fault IDs: 8 and 17) or larger angles ψ to S_{HMAX}. This may reflect that faults active over long time periods are more likely to be misoriented with respect to the current stress field.

We also test the thickness of the seismogenic layer z as a static geometrical factor for particular fault sections (spatial extension of the order of ~100 km) to improve the scaling of M_{MAX}^{obs} by constraining the rupture geometry. As expected from equation (1), M_{MAX}^{obs} associated with each fault increases with the local seismogenic thickness (Figure 1c), although the data dispersion is large. No particular dependence between z and fault orientation ψ is observed. The Dead Sea Transform (ID = 8 in Figure 1c) has unusually large z [*Aldersons et al.*, 2003; *Braeuer et al.*, 2012] even considering that the regional heat flow of approximately 50–60 mW/m^2 [*Mohsen et al.*, 2006] is slightly lower than the average global value. This fault also has unusually low $\psi \approx 25°$ considering its age of activity. The Chaman Fault (ID = 7 in Figure 1c) also displays a large seismogenic depth, although here the accuracy of earthquake hypocenters is limited. Most of the events with unknown magnitude type are placed at the lower bound of the scaling.

For faults representing 75% of the analyzed data set (hereafter referred as "type A" faults), the seismic scalar moment M_0 follows a power law distribution with C_d. Accordingly, M_{MAX}^{obs} increases from M_W 6.5 for faults with few tens of kilometers of C_d to M_W 8.1 with $C_d \approx 400$ km. A magnitude of $\sim M_W 8$ appears to be an approximate observed upper bound. The increase with cumulative displacement is well documented for M_W (better constrained but fewer data) and is also observed for all available magnitude data (Figure 2a). All Type A faults other than the Newport-Inglewood Fault (ID: 19) have $C_d > 10$ km. Therefore, for faults with $C_d > 10$ km, the cumulative displacement may serve as a proxy to estimate M_{MAX}^{obs}. The remaining 25% of the fault sections (hereafter referred as "fault type B") also scale with C_d, but they tend to rupture in larger earthquakes compared to type A faults. For most of these faults, M_W could be inferred with similar quality, suggesting that the separation into two fault populations does not result from worse magnitude quality. In general, type A faults have an average slip rate >5 mm/yr and therefore could be considered as interplate faults [*Scholz et al.*, 1986]. In contrast, all type B faults have $C_d > 10$ km and typically slip rate <5 mm/yr, producing events that are intraplate or at some distance from a plate boundary. Exceptions are the Fairweather Fault (ID = 12) and the Whittier-Elsinore fault (ID = 26), which are placed in the opposite fault type than expected by their slip rates. Large variations between the current and long-term slip rates could provide a potential explanation on why these two faults are located in opposite populations. In addition, most of type A faults are oriented outside the range $\psi \approx [40 - 50]°$ (with the exception of the North Anatolian Fault Zone, ID = 20), while type B faults are mostly oriented at about 45° with respect to S_{HMAX}.

Plotting M_{MAX}^{obs} versus the product $C_d \cdot z$ improves the regression coefficient R of faults type A from ~0.78 to ~0.84, which is again separated from faults type B (Figure 2b). Faults with relatively large M_{MAX}^{obs} (type B) include the Atera, Neodani, Atotsugawa, and Tanna faults from Japan, as well as the San Miguel (Baja California), Camp Rock (Eastern California Shear Zone), and Fairweather (Alaska) faults (Figure 2b). For both fault types, we show regression lines including all data available as well as only M_W data. Most magnitude data from the different faults lie within two linear regressions to the minimum and maximum magnitudes, respectively (green dashed lines in Figure 2b). Using all available data from the faults type A data set, we obtain the empirical relation $M_0 = 10^{17.1} (zC_d)^1$. Interestingly, the slopes of the two fault populations are relatively similar with an offset in the scalar moment.

Given that C_d and L_f are related, we check also the relation between M_{MAX}^{obs} and $z \cdot L_f$ assuming a constant seismogenic depth z within each region. Here the Wairau Fault (ID = 24) has been grouped with the Alpine Fault (ID = 1) since they form a rather continuous fault zone (see Figure S1 in the supporting information). In this case, 80% of the fault data set displays a scaling between M_{MAX}^{obs} and $L_f \cdot z$ (Figure 2c). No clear separation between fault populations A and B is observed, but most data are bounded by the regressions performed to the minimum and maximum magnitudes of type A faults. Two of the seven faults from type B (Figure 2b) are
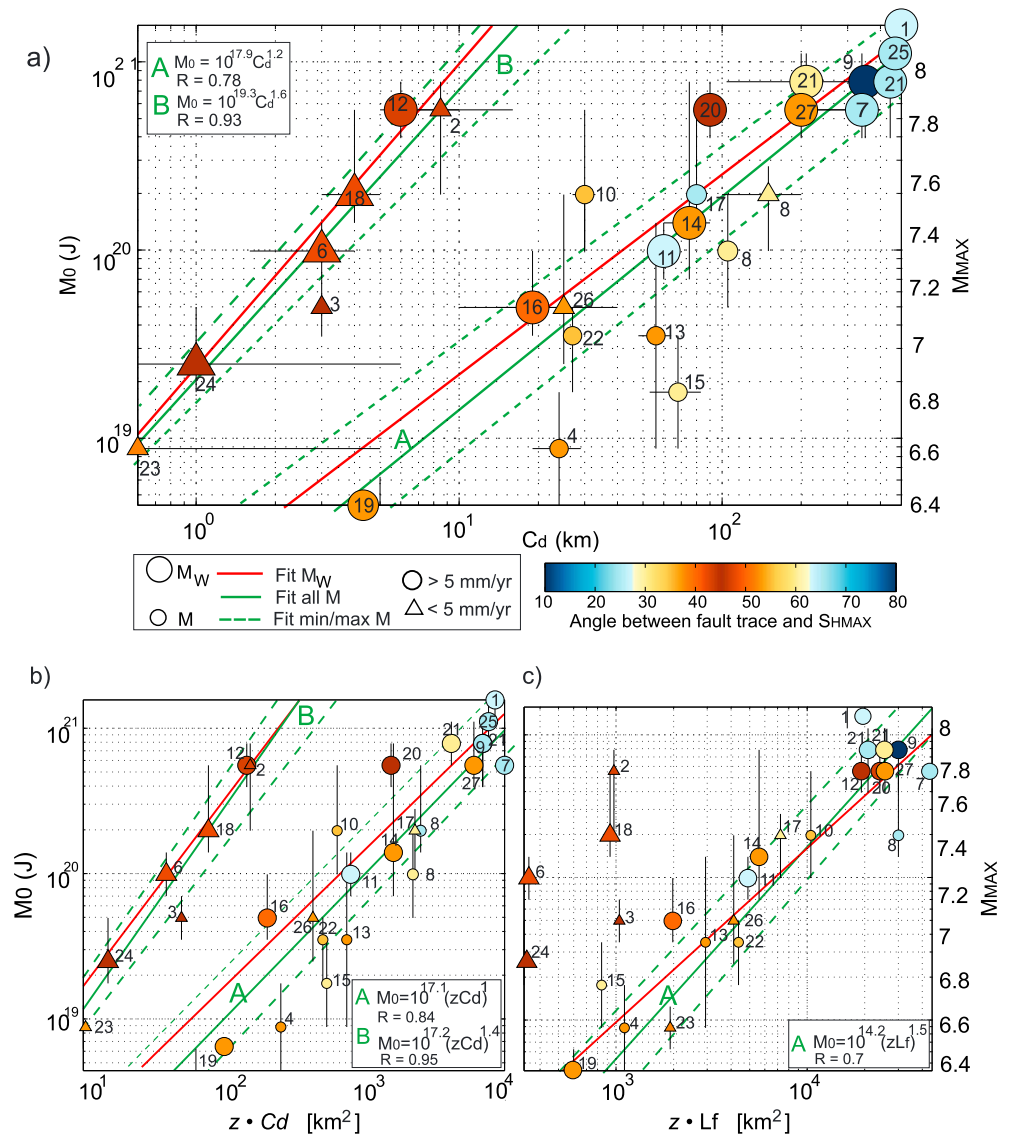
Figure 2. (a) Relation between cumulative displacement (C_d), moment magnitude (M_0), and maximum magnitude (M_{MAX}^{obs}). Vertical error bars are the estimated magnitude uncertainty, while horizontal error bars represent the uncertainty in the cumulative displacement measurement (when available). Color is encoded with the angle ψ between the fault trace and S_{HMAX}. (b) Plot of M_{MAX}^{obs} versus cumulative displacement (C_d) times seismogenic thickness (z). Note that two distinct fault populations exist with a significant offset in magnitude (fault types A and B). (c) Scaling between M_{MAX}^{obs} and total measured fault length (L_f) times seismogenic thickness (z). For all figures, numbers beside each point are the fault identifiers (ID) as listed in Table S1. Size of the data points, lines, and symbols represent the same as in Figure 1. The regression lines plotted in Figure 2c only refer to faults of type A.

now included in the main fault population with log($L_f \cdot z$) scaling with M_{MAX}. These are the Fairweather and San Miguel faults (IDs: 12 and 23), whose small C_d in relation to L_f was previously noted (Figure 1b). Still, five type B faults out of 26 with fault area of approximately (10^3 km^2) also have a larger M_{MAX}^{obs} in relation to the log $L_f \cdot z$ scaling of most data. These five outlier faults (Figure 2c) all have $C_d > 10$ km and slip rate $s_r < 5$ mm/yr: the Japanese faults Atera, Atotsugawa, Neodani, and Tanna and the Camp Rock Fault, Eastern California Shear Zone (IDs: 2, 3, 18, 24 and 6). As expected, the trends of the seismic moment versus C_d and mapped fault length L_f are similar as C_d and L_f are related (Figure 1b) [see also *Scholz*, 2002].

In general, earthquakes with estimated moment magnitudes and those with unknown magnitude types show similar trends. However, many events with unknown magnitude type display lower magnitudes
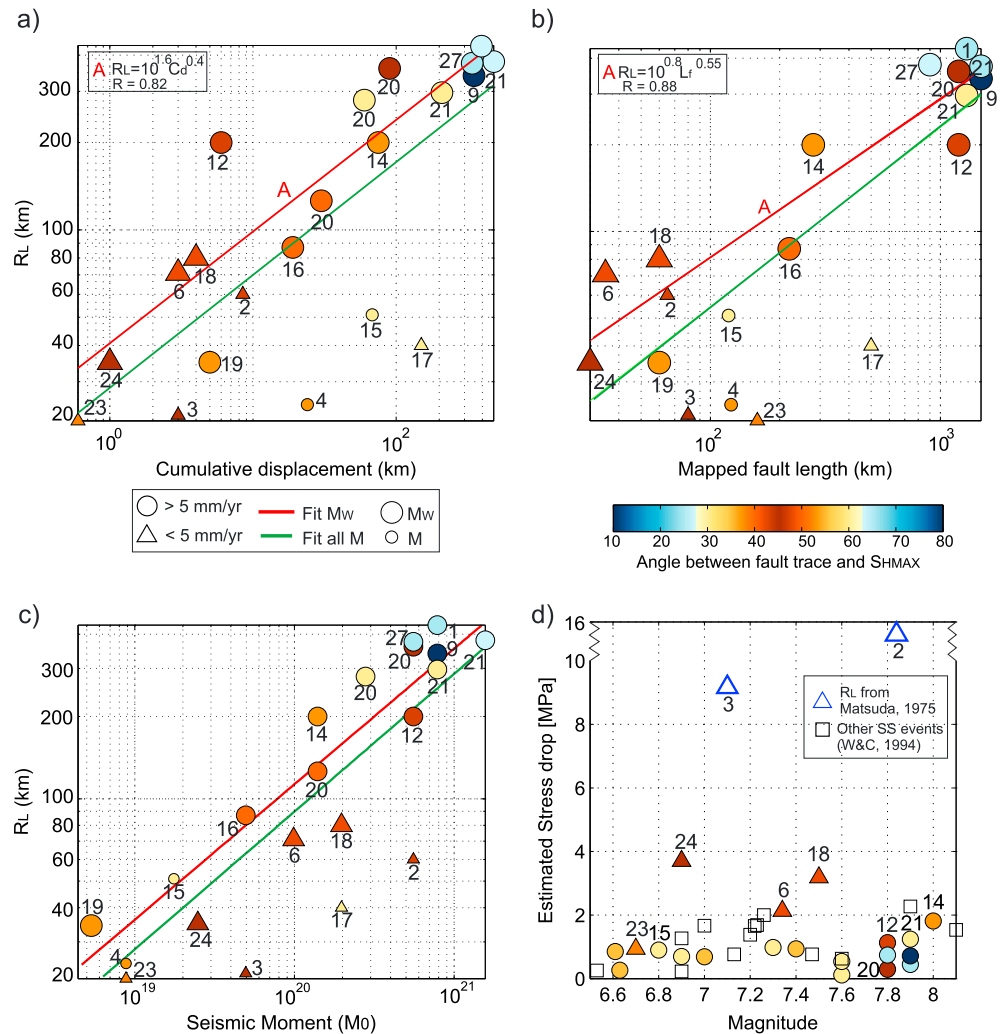
Figure 3. (a) Earthquake rupture length R_L as a function of cumulative displacement (data mostly from *Wells and Coppersmith* [1994]). (b) Earthquake rupture length R_L as a function of total mapped fault length. (c) Earthquake rupture length R_L and observed seismic moment. (d) Estimated stress drop as a function of magnitude including all strike slip earthquakes from *Wells and Coppersmith* [1994] catalog (black squares). Color is encoded with the angle ψ between fault trace and S_{HMAX} when it is known. Coseismic slips for the Atera and Atotsugawa faults (IDs: 2 and 3) estimated following *Matsuda* [1975] are marked with dark blue triangles. Size of the symbols, symbols, and lines represent the same as in Figures 1 and 2.

(Figures 1c and 3a), suggesting that such events may be slightly underestimated. As mentioned, it is also important to keep in mind that the largest observed earthquakes on a fault may underestimate the largest possible events due to the short observation period.

4. Discussion

Analysis of geometrical properties, stress parameters, and observed maximum magnitude from 29 major continental strike-slip fault sections worldwide reveals that M_{MAX}^{obs} observed in 75% and 80% of these faults scales logarithmically with cumulative displacement and mapped fault length, in combination with the seismogenic thickness. Most of the faults (type A) have slip rate >5 mm/yr (~interplate events). The remaining 20–25% (fault type B) also display scaling between M_{MAX}^{obs} and cumulative displacement, although the observed M_{MAX}^{obs} are larger. These faults have $C_d < 10$ km slip rate <5 mm/yr (events not directly at the plate boundary), and their fault trace forms a comparatively small angle of 45° with respect to the maximum horizontal stress direction.

To further explore the suggested scaling relations, we test which factors contributing to the scalar moment (equation (1)) likely correlate with C_d or L_f. For earthquakes that occurred within the instrumental period, the rupture length is found to increase with cumulative displacement as $R_L = 10^{1.5} C_d 0.4$ (Figure 3a). Since C_d and L_f are related (Figure 1b), an equivalent relation is observed between R_L and L_f (Figure 3b). This suggests that the maximum observed earthquake rupture length increases as a fault evolves and increases in length. Since rupture length R_L and slip $\Delta\mu$ are also related [e.g., *Scholz*, 2002; *Ben-Zion*, 2008], we expect the observed scaling between M_{MAX}^{obs} and C_d with a slope of about 1, as observed for faults type A (Figure 2). Fault evolution with increasing fault length L_f and cumulative displacement C_d reduces the structural heterogeneity. The power law fit between earthquake rupture length and fault length (Figure 3b) suggests that they are related through $R_L \approx \sqrt{L_f}$, indicating that total fault length grows much faster than maximum rupture length. This indicates that fault heterogeneities may persist through many seismic cycles although the fault may continue to grow in length (e.g., as observed for the North Anatolian Fault Zone). Figure 3a does not show any difference between type A and B faults, suggesting that R_L is comparable for both fault types.

It is well known that the earthquake magnitude depends logarithmically on rupture length (R_L) (equation (1)). The available rupture lengths corresponding to the M_{MAX}^{obs} earthquakes (mostly from *Wells and Coppersmith* [1994]) are displayed in Figure 3c with their seismic moment. The R_L of the five type B earthquakes which do not scale with the mapped fault length (IDs: 2, 3, 6, 18, and 24) has comparable or smaller rupture length than other events with similar seismic moment. Similarly, Figure 1c shows that the seismogenic thickness of the regions associated with these earthquakes (representing the rupture width) is not larger than other earthquakes of similar magnitudes. Therefore, fault area is not the main difference between fault types A and B.

The average coseismic slip $\Delta\mu$ has been estimated in 12 out of the 29 M_{MAX}^{obs} earthquakes, including the 1992 Landers earthquake (ID: 6), the 1891 Nobi earthquake (ID: 18), and the 1930 North-Izu earthquake (ID: 23), which belong to the type B earthquakes not scaling with the L_f. Source parameters from the two remaining earthquakes from type B faults not fitting the scaling with L_f (Atera and Atotsugawa faults, IDs: 2 and 3) are not available since they occurred earlier than the instrumental period. In these cases, the rupture length and corresponding average coseismic slip are estimated following the empirical relation of *Matsuda* [1975] for Japanese faults: $\log R_L(\mathrm{km}) = 0.6M - 2.9$. The resulting $\Delta\mu$ values for these two events are significantly larger than for other earthquakes with similar magnitude. The stress drop $\Delta\sigma$ may be approximately estimated as the ratio between $\Delta\mu$ and a characteristic length $\widetilde{L}$ multiplied by the rigidity:

$$\Delta\sigma \approx \mu\Delta\mu\widetilde{L}. \tag{2}$$

For the considered earthquakes on strike-slip faults, one possibility for estimating the characteristic length $\widetilde{L}$ is to use the W source model [*Scholz*, 1982] where the stress drop and slip are determined by the fault width. However, both data and model simulations suggest that the slip continues to grow with rupture length $R_L > W$ [e.g., *Wells and Coppersmith*, 1994; *Wesnousky*, 2008; *Hillers and Wesnousky*, 2008]. In such cases, using $\widetilde{L} = (R_L + W)/2$ would be more consistent with the constant stress drop model, whereas the W source model would imply stress drops that increase for events with $R_L > W$. In the following we estimate $\Delta\sigma$ from equation (2) with $\widetilde{L} = (R_L + W)/2$ and a constant rigidity value of 30 GPa.

While this technique provides only approximate $\Delta\sigma$ values, and more accurate methods may give better estimates, we observe that events from faults type B have comparatively large stress drops than events from type A faults, as well as other strike-slip earthquakes with same the magnitude from the *Wells and Coppersmith* [1994] data set (Figure 3d). An alternate analysis using the W model leads to larger stress drop differences between these two types of events (Figure S2). Larger stress drops are found generally for events on type B faults with average slip rates lower than 5 mm/yr (i.e., not main plate boundary faults). Although these stress drop estimates are rough, the values for the Tanna and Neodani faults are in good agreement with reported stress drops for central Japan [*Oth*, 2013]. High stress drop was also reported for the 1992 Landers earthquake [*Sieh et al.*, 1993] and for events on various intraplate faults [*Kanamori and Anderson*, 1975; *Scholz et al.*, 1986]. These faults usually have relatively low slip rates, long recurrence times, and large frictional strength [*Cao and Aki*, 1986]. The relatively short lengths of faults associated with shallow inland strike-slip events have also been noted before [*Kikuchi*, 1992; *Tsutsumi and Okada*, 1996]. Thus, the larger stress drops on type B faults may explain the shift in magnitudes between fault types A and B with given cumulative offset. Larger stress drops for type B faults suggest that progressive smoothing of a fault as it evolves with increasing

displacement could reduce the average stress drop (as proposed by *Manighetti et al.* [2007]) and possibly M_{MAX} as observed in this study for the more developed type A faults.

From the orientation of the faults with respect to S_{HMAX}, type B faults appear to be more favorably oriented and have larger resolved shear stress. The range of angles from type A faults varies between 25° and 78°. From the analyzed type A faults, there are six faults which have larger angle than 60°, which makes them unfavorably oriented with respect of the stress field assuming a coefficient of friction of 0.6. However, this is based on the strike of the fault and assuming that the fault dip is ≈90°. If the fault dip is not close to 90° (e.g., the Alpine Fault), their potential to be reactivated may increase.

Lastly, in most cases, the end points of strike-slip earthquakes are bound by the tips of active fault segments [*Wesnousky*, 2006]. For fault type B, the mapped surface length L_f of a segment having M_{MAX} event is similar or smaller than the earthquake rupture length R_L. Thus, large earthquakes associated with these faults activate multiple segments, which are often mapped as individual faults but are sufficiently close as to be activated in a single rupture. This is consistent with previous studies of combined rupture of multiple individual segments [e.g., *Segall and Pollard*, 1980; *Manighetti et al.*, 2007]. For the type B fault data analyzed here at least three large events are attributed to the rupture of more than one individual small fault. The 1992 Landers earthquake was related to the Camp Rock Fault, but it ruptured a total of five faults [*Sieh et al.*, 1993]. The 1891 Nobi earthquake has been compared with the Landers earthquake due to the rupture of up to three faults including the Neodani Fault [*Kaneda and Okada*, 2008]. Similarly, the 1930 North-Izu earthquake occurred in the North-Izu Fault System, in which the main activated fault was the Tanna Fault.

In summary, type B faults represent individual (named) faults, but some may be activated together in a single rupture, creating a larger earthquake than would be expected from each fault separately. These short faults may sustain energetic ruptures with larger stress drops than observed for type A faults. Higher than average stress drops will facilitate propagation through step overs into adjacent fault segments, resulting in a larger earthquake.

5. Conclusions

The relation between maximum observed earthquake magnitude and different geometrical and stress properties of strike-slip faults is analyzed to investigate whether these properties can help in constraining M_{MAX}^{obs} at these faults. Despite combination of faults with bounded and unbounded tips, a dependency is observed between their mapped fault length and their cumulative displacement. About 75% of the analyzed fault sections (type A) have a logarithmic scaling between M_{MAX}^{obs} and the product of seismogenic depth and cumulative displacement. These faults typically have slip rates $s_r > 5$ mm/yr (representing interplate faults), cumulative displacements $C_d > 10$ km, and angles $\psi > 50°$ with respect to the regional maximum horizontal stress. Using the total mapped fault length, a similar relation is observed fitting 80% of the total data set. The physical mechanism underlying these correlations may be increasing maximum available earthquake rupture length with cumulative displacement and surface fault length. The remaining 25–20% (depending on the scaling with cumulative displacement or total mapped fault length, respectively) of faults (type B) also scale with the product of seismogenic depth and cumulative displacement, but they have larger M_{MAX}^{obs} than the faults of type A. These type B faults have slip rates lower than 5 mm/yr (i.e., are at some distance from the plate boundary), cumulative displacement $C_d > 10$ km, and they are oriented at approximately 45° with respect to the maximum horizontal stress, suggesting larger resolved shear stress. Earthquakes associated with these faults have comparatively large stress drops than earthquakes from type A faults. The progressive smoothing of the fault as it evolves with cumulative displacement appears to reduce the earthquake stress drops but does not modify the rupture length. The obtained scaling relations, combined with classification of a given fault to type A or B, provide useful information for estimating the largest earthquake on that fault.

References

Albini, P., R. M. W. Musson, A. A. Gomez Capera, M. Locati, A. Rovida, M. Stucchi, and D. Viganò (2013), *Global Historical Earthquake Archive and Catalogue (1000–1903)*, *GEM Tech. Rep.*, GEM Foundation, Pavia, Italy.
Aldersons, F., Z. Ben-Avraham, A. Hofstetter, E. Kissling, and T. Al-Yazjeen (2003), Lower-crustal strength under the Dead Sea basin from local earthquake data and rheological modeling, *Earth Planet. Sci. Lett.*, *214*(1–2), 129–142, doi:10.1016/S0012-821X(03)00381-9.

Ambraseys and Jackson (1998), Faulting associated with historical and recent earthquakes in the Eastern Mediterranean region, *Geophys. J. Int.*, *133*(2), 390–406, doi:10.1046/j.1365-246X.1998.00508.x.

Ben-Menahem, A. (1991), Four thousand years of seismicity along the Dead Sea Rift, *J. Geophys. Res.*, *96*(B12), 20,195–20,216, doi:10.1029/91JB01936.

Ben-Zion, Y. (2008), Collective behavior of earthquakes and faults: Continuum-discrete transitions, progressive evolutionary changes, and different dynamic regimes, *Rev. Geophys.*, *46*, RG4006, doi:10.1029/2008RG000260.

Ben-Zion, Y., and C. G. Sammis (2003), Characterization of fault zones, *Pure Appl. Geophys.*, *160*(3–4), 677–715, doi:10.1007/PL00012554.

Ben-Zion, Y., and L. Zhu (2002), Potency-magnitude scaling relations for southern California earthquakes with $1.0 < M_L < 7.0$, *Geophys. J. Int.*, *148*(3), F1–F5, doi:10.1046/j.1365-246X.2002.01637.x.

Braeuer, B., G. Asch, R. Hofstetter, C. Haberland, D. Jaser, R. El-Kelani, and M. Weber (2012), Microseismicity distribution in the southern Dead Sea basin and its implications on the structure of the basin, *Geophys. J. Int.*, *188*(3), 873–878, doi:10.1111/j.1365-246X.2011.05318.x.

Brodsky, E. E., J. J. Gilchrist, A. Sagy, and C. Collettini (2011), Faults smooth gradually as a function of slip, *Earth Planet. Sci. Lett.*, *302*(1–2), 185–193, doi:10.1016/j.epsl.2010.12.010.

Cao, T., and K. Aki (1986), Effect of slip rate on stress drop, *Pure Appl. Geophys.*, *124*(3), 515–529, doi:10.1007/BF00877214.

Cowie, P. A., and C. H. Scholz (1992a), Growth of faults by accumulation of seismic slip, *J. Geophys. Res.*, *97*(B7), 11,085–11,095, doi:10.1029/92JB00586.

Cowie, P. A., and C. H. Scholz (1992b), Physical explanation for the displacement-length relationship of faults using a post-yield fracture mechanics model, *J. Struct. Geol.*, *14*(10), 1133–1148, doi:10.1016/0191-8141(92)90065-5.

Hanks, T. C., and H. Kanamori (1979), A moment magnitude scale, *J. Geophys. Res.*, *84*(B5), 2348–2350, doi:10.1029/JB084iB05p02348.

Hauksson, E., W. Yang, and P. M. Shearer (2012), Waveform relocated earthquake catalog for southern California (1981 to June 2011), *Bull. Seismol. Soc. Am.*, *102*(5), 2239–2244, doi:10.1785/0120120010.

Hillers, G., and S. G. Wesnousky (2008), Scaling relations of strike-slip earthquakes with different slip-rate dependent properties at depth, *Bull. Seismol. Soc. Am.*, *98*, 1085–1101.

Kanamori, H., and D. L. Anderson (1975), Theoretical basis of some empirical relations in seismology, *Bull. Seismol. Soc. Am.*, *65*(5), 1073–1095.

Kaneda, H., and A. Okada (2008), Long-term seismic behavior of a fault involved in a multiple-fault rupture: Insights from tectonic geomorphology along the Neodani Fault, Central Japan, *Bull. Seismol. Soc. Am.*, *98*(5), 2170–2190, doi:10.1785/0120070204.

Kikuchi, M. (1992), Strain drop and apparent strain for large earthquakes, *Tectonophysics*, *211*(1–4), 107–113, doi:10.1016/0040-1951(92)90054-A.

Kim, Y.-S., and D. J. Sanderson (2005), The relationship between displacement and length of faults: A review, *Earth Sci. Rev.*, *68*(3–4), 317–334, doi:10.1016/j.earscirev.2004.06.003.

Leonard, M. (2010), Earthquake fault scaling: Self-consistent relating of rupture length, width, average displacement, and moment release, *Bull. Seismol. Soc. Am.*, *100*(5A), 1971–1988.

Manighetti, I., M. Campillo, S. Bouley, and F. Cotton (2007), Earthquake scaling, fault segmentation, and structural maturity, *Earth Planet. Sci. Lett.*, *253*(3–4), 429–438, doi:10.1016/j.epsl.2006.11.004.

Matsuda, T. (1975), Magnitude and recurrence interval of earthquakes from a fault, *Zishin*, *2*(28), 269–283.

Mohsen, A., R. Kind, S. V. Sobolev, M. Weber, and the DESERT Group (2006), Thickness of the lithosphere east of the Dead Sea Transform, *Geophys. J. Int.*, *167*(2), 845–852, doi:10.1111/j.1365-246X.2006.03185.x.

Oth, A. (2013), On the characteristics of earthquake stress release variations in Japan, *Earth Planet. Sci. Lett.*, *377–378*, 132–141, doi:10.1016/j.epsl.2013.06.037.

Pacheco, J. F., and L. R. Sykes (1992), Seismic moment catalog of large shallow earthquakes, 1900 to 1989, *Bull. Seismol. Soc. Am.*, *82*(3), 1306–1349.

Parsons, T. (2004), Recalculated probability of $M \geq 7$ earthquakes beneath the Sea of Marmara, Turkey, *J. Geophys. Res.*, *109*, B05304, doi:10.1029/2003JB002667.

Petersen, M. D., et al. (2015), Incorporating induced seismicity in the 2014 United States National Seismic Hazard Model—Results of 2014 workshop and sensitivity studies, *U.S. Geol. Surv. Open File Rep.*, *2015–1070*, 69 pp., doi:10.3133/ofr20151070.

Scholz, C. (1982), Scaling laws for large earthquakes: Consequences for physical models, *Bull. Seismol. Soc. Am.*, *72*, 1–14.

Scholz, C. H. (2002), *The Mechanics of Earthquakes and Faulting*, 2nd ed., Cambridge Univ. Press, Cambridge, U. K., doi:10.1017/S0016756803227564.

Scholz, C. H., C. A. Aviles, and S. G. Wesnousky (1986), Scaling differences between large interplate and intraplate earthquakes, *Bull. Seismol. Soc. Am.*, *76*(1), 65–70.

Scordilis, E. M. (2006), Empirical global relations converting M_S and m_b to moment magnitude, *J. Seismol.*, *10*(2), 225–236, doi:10.1007/s10950-006-9012-4.

Segall, P., and D. D. Pollard (1980), Mechanics of discontinuous faults, *J. Geophys. Res.*, *85*(B8), 4337–4350, doi:10.1029/JB085iB08p04337.

Shaw, B. E. (2009), Constant stress drop from small to great earthquakes in magnitude-area scaling, *Bull. Seismol. Soc. Am.*, *99*(2A), 871–875, doi:10.1785/0120080006.

Sieh, K., et al. (1993), Near-field investigations of the landers earthquake sequence, April to July 1992, *Science*, *260*(5105), 171–176, doi:10.1126/science.260.5105.171.

Stirling, M. W., S. G. Wesnousky, and K. Shimazaki (1996), Fault trace complexity, cumulative slip, and the shape of the magnitude-frequency distribution for strike-slip faults: A global survey, *Geophys. J. Int.*, *124*(3), 833–868, doi:10.1111/j.1365-246X.1996.tb05641.x.

Strasser, M., F. S. Anselmetti, D. Fäh, D. Giardini, and M. Schnellmann (2006), Magnitudes and source areas of large prehistoric northern Alpine earthquakes revealed by slope failures in lakes, *Geology*, *34*(12), 1005–1008, doi:10.1130/G22784A.1.

Tchalenko, J. S. (1970), Similarities between shear zones of different magnitudes, *Geol. Soc. Am. Bull.*, *81*(6), 1625–1640, doi:10.1130/0016-7606(1970)81[1625:SBSZOD]2.0.CO;2.

Tsutsumi, H., and A. Okada (1996), Segmentation and Holocene surface faulting on the Median Tectonic Line, southwest Japan, *J. Geophys. Res.*, *101*(B3), 5855–5871, doi:10.1029/95JB01913.

United States Geological Survey (2008), *Probabilistic Seismic Hazard Programme*, United States Geol. Surv.

Utsu, T. (1999), Representation and analysis of the earthquake size distribution: A historical review and some new approaches, *Pure Appl. Geophys.*, *155*(2–4), 509–535, doi:10.1007/s000240050276.

Waldhauser, F., and D. P. Schaff (2008), Large-scale relocation of two decades of Northern California seismicity using cross-correlation and double-difference methods, *J. Geophys. Res.*, *113*, B08311, doi:10.1029/2007JB005479.

Wechsler, N., Y. Ben-Zion, and S. Christofferson (2010), Evolving geometrical heterogeneities of fault trace data, *Geophys. J. Int.*, *182*(2), 551–567, doi:10.1111/j.1365-246X.2010.04645.x.

Wells, D. L., and K. J. Coppersmith (1994), New empirical relationships among magnitude, rupture length, rupture width, rupture area, and surface displacement, *Bull. Seismol. Soc. Am.*, *84*(4), 974–1002.

Wesnousky, S. G. (1988), Seismological and structural evolution of strike-slip faults, *Nature*, *335*(6188), 340–343, doi:10.1038/335340a0.

Wesnousky, S. G. (2006), Predicting the endpoints of earthquake ruptures, *Nature*, *444*(7117), 358–360, doi:10.1038/nature05275.

Wesnousky, S. G. (2008), Displacement and geometrical characteristics of earthquake surface ruptures: Issues and implications for seismic hazard analysis and the process of earthquake rupture, *Bull. Seismol. Soc. Am.*, *98*, 1609–1632.